Electronic Supplementary Information

Single-Component Small-Molecule White Light Organic Phosphors

Ning-Ning Zhang,[a,b] Cai Sun,[a,b] Xiao-Ming Jiang,[a] Xiu-Shuang Xing,[a,b] Yong Yan,[a,b] Li-Zhen Cai,[a] Ming-Sheng Wang,[a,b,*] & Guo-Cong Guo[a,*]

[a]State Key Laboratory of Structural Chemistry, Fujian Institute of Research on the Structure of Matter, Chinese Academy of Sciences, Fuzhou, Fujian 350002, P. R. China. E-mail: mswang@fjirsm.ac.cn; gcguo@fjirsm.ac.cn.
[b]University of Chinese Academy of Sciences, Beijing 100039, P. R. China.

Table of Contents

1 Experimental Procedures

1.1 Materials.

4-acetylphenyl azide was prepared according to the previously reported procedure.[1] Water was used after deionization and distillation. All the other chemicals were purchased commercially and used without further treatment.

Caution! It should be careful of using azide compounds, which are potentially hazardous. They should be handled with plastic spoon.

1.2 Methods.

Infrared (IR) data were obtained by a PerkinElmer Spectrum One FT-IR spectrophotometer over the scope 4000−400 cm^{-1} with the pure KBr pellets as the baseline. ^{1}H NMR and ^{13}C NMR spectra were measured at room temperature by an Advance III NMR spectrometer operating at 400 MHz. Elemental analyses of C, H, and N were performed on an Elementar Vario EL III microanalyzer. Mass spectra were recorded with DECAX-30000 LCQ Deca XP Ion Trap Mass Spectrometry. Thermogravimetry (TG) analyses were done on a NETZSCH STA 449C simultaneous thermal analyzer with Al_2O_3 crucibles under N_2 (20 mL·min^{-1}) at a heating rate of 10 K·min^{-1}. Powder X-ray diffraction (PXRD) patterns were collected at room temperature on a Rigaku MiniFlex II diffractometer using Cu $K\alpha$ radiation (λ = 1.5406 Å). Simulated PXRD patterns were derived from the Mercury Version 3.5.1 software using the X-ray single crystal diffraction data. UV–Vis absorption spectra were measured in the reflectance mode at room temperature on a Perkin-Elmer Lambda 900 UV/vis/NIR spectrophotometer with an integrating sphere attachment and $BaSO_4$ as a reference. Photoluminescent spectra were recorded on a single-grating Edinburgh EI920 fluorescence spectrometer equipped with a 450 W Xe lamp. Lifetimes were measured on an Edinburgh FLS980 UV/V/NIR Fluorescence Spectrometer. Quantum yields were measured on an Edinburgh FLS920 UV/V/NIR fluorescence spectrometer using an integrating sphere. The detailed experiment for white-light LEDs was as following: Firstly, we obtained the concentrated DMF solutions of **1** and **2**, and then added 5 wt % PMMA. Finally, the solutions drop-casted to the UV LEDs uniformly and then dried in air.

Defect study for photoluminescence. According to the methods described in the literature,[2] we probed the impact of defect concentration on the photoluminescence, taking compound **2** for example. The crystals of **2**, obtained by recrystallization from ethanol at 25 °C, was annealed at 150 °C (below the decomposition temperature; Fig. S2) for 1 d. A powder X-ray diffraction (PXRD) study showed that the crystallinity in the sample increased, but the photoluminescent emission profiles were almost the same before and after annealing (Fig. S3). The emission spectra of crystals grown from solution at 25 and 0 °C (Fig. S4) and crystals before and after crushing (Fig. S5) were within experimental error, indicating that differences in crystallization rates and size at these temperatures do not affect the emission. If the emission arises from permanent defects, there will be PL saturation as these traps become filled. We measured the PL emission spectra at λ_{ex} = 420 nm as the increase of excitation power density. PL intensities at 560 nm increase linearly with excitation power density from 3 to 235 mW/cm^2 using laser at 295 K (Fig. S6), without signs of

PL saturation. This linear behavior suggests that emission does not arise from permanent material defects. We also see no change in emission band shape throughout this experiment (Fig. S6 inset), indicating that different emissive defect sites are not accessed at different excitation intensities. These results indicate that the solid-state photoluminescence of **2** is intrinsic and does not arise from the defects. The PL signals at λ_{ex} = 420 nm were detected with an Andor DU420A-BR-DD CCD array detector.

X-ray crystallographic study. The intensity data sets were collected on an Agilent Technologies SuperNova Dual Wavelength CCD diffractometer with graphite-monochromated Cu *K*α radiation (λ = 0.71073 Å) using the $\omega-2\theta$ scan technique and reduced by the CrysAlisPro software.[3]The data set were corrected for Lorentz and polarization factors, as well as for absorption by the numerical method. The structures were solved by the direct method and refined by full-matrix least squares on F^2 using the Siemens SHELXTLTM Version 5 package of crystallographic software,[4] with anisotropic thermal parameters for all non-hydrogen atoms. Hydrogen atoms were added geometrically and refined using the riding model. By using the program PLATON,[5] the structures were also checked for possible missing symmetry and none was found. Crystal data and structure refinement results for **1** and **2** are summarized in Table S3.

The entries of CCDC-1537756, 1526952 contain the supplementary crystallographic data for **1** and **2**, respectively. These data can be obtained free of charge at http://www.ccdc.cam.ac.uk/conts/retrieving.html or from the Cambridge Crystallographic Data Centre, 12, Union Road, Cambridge CB2 1EZ, U.K. Fax: (Internet) +44-1223/336-033. E-mail: deposit@ccdc.cam.ac.uk.

Calculation of UV–Vis absorption spectra. The calculation was conducted using the Gaussian 09 package.[6] We chose the widely used B3LYP[7] as an exchange correlation function in view of its good compromise between accuracy and computational cost. UV–Vis absorption spectra of the monomers of **1** and **2** in the *N*,*N*-dimethylformamide solution were achieved by time-dependent density functional theory (TD-DFT) calculation at the B3LYP/6-31G(d,p) level using optimized geometry. Vibrational analysis was performed to confirm each optimized stationary point to be a minimum. TD-DFT calculations at the B3LYP/6-31G+(d,p) level[8] also produced the UV–Vis absorption spectra of the monomer and different aggregates in the crystals without optimization. The UV–Vis absorption spectra were dealt with the GaussView 5.0 software, with the peak half-width at half height being set as 0.1 eV for Figs. 5e, 5f, and S14 and 0.333 eV for Fig. S8.

Calculation of intermolecular interactions. To obtain plots of the electron density (ρ) and reduced density gradient ($s = 1/(2(3\pi^2)^{1/3})|\nabla\rho|/\rho^{4/3}$), density-functional theory calculations were performed for a selected set of **1** and **2**.[9] Calculations were performed with the B3LYP functional[7] and the 6-31G* basis set, using the Gaussian 09 program.[6] The results were analyzed by Multiwfn.[10]

Calculation of DOS. The calculation models for **1** and **2** were built directly from their single-crystal X-ray diffraction data. The electronic structure calculations based on DFT were performed using the CASTEP package.[11] The exchange-correlation energy was described by the revised Perdew−Burke−Eruzerhof (RPBE) functional within the generalized gradient approximation (GGA).[12] The norm conserving pseudopotentials were chosen to modulate the electron−ion interaction.[13] The orbital electrons of C $2s^22p^2$, H $1s^1$, N $2s^22p^3$, and O $2s^22p^4$ were treated as valence electrons. The plane-wave cutoff energy was 830 eV, and the threshold of 5×10^{-7} eV was set for the self-consistent field convergence of the total electronic energy. The numerical integration of the Brillouin zone was performed using 4 × 1 × 1 and 3 × 3 × 1 Monkhorst−Pack *k*-point meshes for **1** and **2**, respectively. The Fermi level was selected as the reference and set at 0 eV by default.

Calculations of linear optical properties described in terms of the complex dielectric function $\varepsilon = \varepsilon^{Re} + i\varepsilon^{Im}$ were also made in this work. The imaginary part of the dielectric function $\varepsilon^{Im}(\omega)$ was given in the following equation:

$$\varepsilon^{Im}(\omega) = 4\left(\frac{\pi e}{m\omega}\right)^2 \sum_{v,c}\int_{BZ} 2dk\,/(2\pi)^3 |e\cdot M_{cv}(k)|^2 \delta(E_c(k') - E_v(k) - \hbar\omega)$$

where the symbol S is a sum over the valence bands (*v*) and conduction bands (*c*), the *ω* is optical frequency, the m is electron mass, the symbol ∫ is an integration over *k* vectors in Brillouin zone (*BZ*), the $e\cdot M_{cv}(k)$ is an electron transition moment between the conduction and valence bands at the *k* point, and the *d* function is an energy difference between the conduction and valence bands at the *k* point with absorption of a quantum *ħω*.

The Kramers–Kronig transform was used to obtain the real part $\varepsilon^{Re}(\omega)$ of the dielectric function:

$$\varepsilon^{Re}(\omega) = 1 + \frac{2}{\pi} p \int_0^\infty \frac{\omega' \varepsilon^{Im}(\omega')}{\omega'^2 - \omega^2} d\omega',$$

where *p* in front of the integral means the principal value. The absorbance $\alpha(\omega)$ was given in the following equation:[14]

$$\alpha(\omega) = \frac{\varepsilon^{Im}(\omega)\omega}{n(\omega)C},$$

where *C* and $n(\omega)$ are the velocity of light and refractive index, respectively. The $n(\omega)$ was expressed as follow:

$$n(\omega) = \frac{1}{\sqrt{2}}\left[(\varepsilon^{Re}(\omega)^2 + \varepsilon^{Im}(\omega)^2)^{1/2} + \varepsilon^{Re}(\omega)\right]^{1/2}.$$

The smearing width was set as 0.05 eV for Figs. 4a, 4c and 0.5 eV for Figs. 4b, 4d. Other parameters were set as default.

1.3 Synthesis.

Compound 1 was prepared by the copper-catalyzed azide–alkyne click (CuAAC) reaction.[15] The synthetic process is shown in supporting information (Scheme S1). Typically, 4-acetylphenyl azide (5 mmol, 0.815 g), propionic acid (5 mmol, 0.31 mL), sodium ascorbate (VC; 0.5 mmol, 0.099 g), and $CuSO_4$ (0.06 mmol, 0.010 g) were dissolved in 25 mL of a 4:1 DMSO/water mixture. The solution was stirred at room temperature for 2 d, and then poured into 100 mL of ice-cold water. The white precipitate of 1-(4-acetylphenyl)-4-carboxyl-1,2,3-triazole (**1M**) was isolated by filtration, washed with vast cold water, and then dried in air. Yield for **1M**: 82% (based on 4-acetylphenyl azide). IR (KBr, cm^{-1}) : 3143 w, 2928 w, 2621 w, 2560 w, 1709 s, 1659 s, 1604 s, 1549 m, 1517 w, 1445 m, 1407 m, 1385 s, 1368 m, 1302 w, 1280 s, 1264 m, 1242 m, 1198 w, 1165 m, 1028 m, 984 m, 974 m, 893 w, 843 m, 822 w, 772 m, 732 w, 631 w, 591 m, 561 w, 520 w, 500 w, 480 w. ^{1}H-NMR (400 MHz, d_6-DMSO, 25 °C): δ = 13.44 (s, 1H, -COOH), 9.55 (s, 1H, triazole-H), 8.10 (m, 4H, Ph-H), 2.65 (s, 3H, $-CH_3$). ^{13}C-NMR (400 MHz, d_6-DMSO, 25 °C): δ = 197.46, 137.21, 130.50, 120.77, 27.36. Calcd (%) for **1**: C, 57.14; N, 18.17; H, 3.92. Found (%): C, 57.08; N, 18.38; H, 3.92. MS (ESI$^+$, DMSO, *m/z*): Calcd for [*M*–H]$^-$, 230.211; found, 230.057.

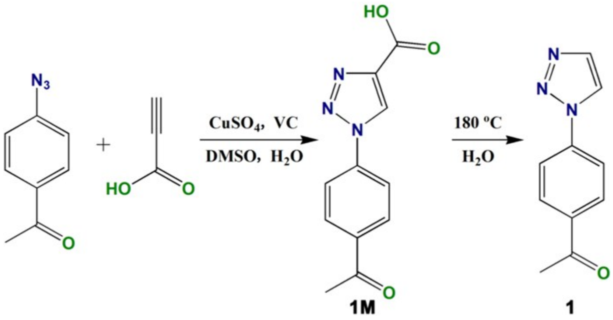

Scheme S1. Preparation of **1**

1 mmol of **1M** and 10 mL of H_2O were sealed into a 25 mL poly(tetrafluoroethylene)-lined stainless steel autoclave and then heated at 180 °C under autogenous pressure and kept at that temperature for 12 h. A powder sample of **1** was gotten by filtration. Yellow flake crystals of **1** were grew by evaporation of an ethanol solution of the powder, which was previously heated at 120 °C for 4 h in an autoclave and then cooled to room temperature. Yield for **1**: 90% (based on **1M**). IR (KBr, cm^{-1}) : 3145 w, 3109 w, 1672 s, 1605 s, 1512 m, 1409 m, 1361 m, 1325 w, 1303 w, 1263 s, 1237 s, 1179 m, 1138 w, 1116 w, 1076 w, 1028 s, 984 m, 957 m, 837 s, 788 s, 757 w, 620 s, 593 s, 522 w, 495 w, 451 w, 424 w. ^{1}H-NMR (400 MHz, d_6-DMSO, 25 °C, Fig. S20): δ = 8.98 (s, 1H, triazole-H), 8.18 (d, J = 8 Hz, 2H, Ph-H), 8.11 (d, J = 8 Hz, 2H, Ph-H), 8.04 (s, 1H, triazole-H), 2.65 (s, 3H, -CH_3). ^{13}C-NMR (400 MHz, d_6-DMSO, 25 °C): δ = 197.45, 140.11, 136.77, 135.28, 130.55, 123.90, 120.30, 27.31. Calcd (%) for **1**: C, 64.16; N, 22.45; H, 4.85. Found (%): C, 64.36; N, 22.55; H, 4.80. MS (ESI$^+$, DMSO, *m/z*, Fig. S22): Calcd for [*M*+H]$^+$, 188.209; found, 188.082. A TG analysis showed that the crystalline sample of **1** is stable up to 156 °C under N_2 atmosphere (Fig. S2).

Compound 2: The preparation of compound **2** was completely according to reported procedures.[16] Yellow flake crystals of **2** were grew by evaporation of an ethanol solution of the powder, which was previously heated at 120 °C for 4 h in an autoclave and then cooled to room temperature. Calcd (%) for **2**: C, 57.14; N, 22.21; H, 3.73. Found (%): C, 56.91; N, 22.08; H, 3.92. IR (KBr, cm^{-1}) : 3150 w, 3118 w, 2816 w, 2670 w, 2539 w, 1684 s, 1600 s, 1521 m, 1449 m, 1418 m, 1319 s, 1293 s, 1230 s, 1173 w, 1110 w, 1032 s, 980 m, 948 w, 860 m, 797 m, 766 s, 687 m, 552 m, 500 w. ^{1}H-NMR (400 MHz, d_6-DMSO, 25 °C, Fig. S21): δ = 13.26 (s, 1H, -COOH), 8.96 (s, 1H, triazole-H), 8.15 (d, J = 8 Hz, 2H, Ph-H), 8.08 (d, J = 8 Hz, 2H, Ph-H), 8.03 (s, 1H, triazole-H). ^{13}C-NMR (400 MHz, d_6-DMSO, 25 °C): δ = 166.96, 140.01, 135.24, 131.55, 123.86, 120.33. MS (ESI$^-$, DMSO, *m/z*, Fig. S23): Calcd for [*M*–H]$^-$, 188.166; found, 188.046. A TG analysis showed that **2** is stable up to 200 °C under N_2 atmosphere (Fig. S2).

2 Results and Discussion

Table S1. The CIE coordinates, correlated color temperature (CCT), color rendering index (CRI) and quantum yield (Qc) of **1** and **2** under different excitation wavelengths.

		Excitation wavelengths (nm)						Qc
		320	**330**	**340**	**350**	**360**	**370**	
1	**CIE**	(0.36,0.41)	(0.34,0.40)	(0.34,0.40)	(0.33,0.39)	(0.33,0.39)	(0.32,0.38)	2.00%
	CCT	4535	5164	5288	5449	5534	5953	
	CRI	83	82	82	81	83	83	
2	**CIE**	(0.27,0.30)	(0.27,0.30)	(0.28,0.30)	(0.29,0.32)	(0.31,0.35)	(0.31,0.35)	2.04%
	CCT	9998	10058	9637	8164	6258	6218	
	CRI	88	88	88	87	84	83	

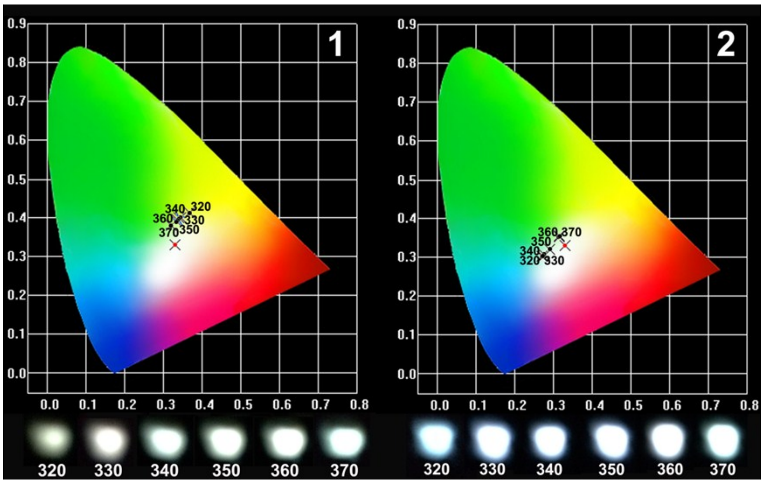

Fig. S1 The CIE coordinates and photoluminescent photographs of **1** and **2** under different excitation wavelengths. Red dots: CIE coordinates for ideal white light, (0.33, 0.33).

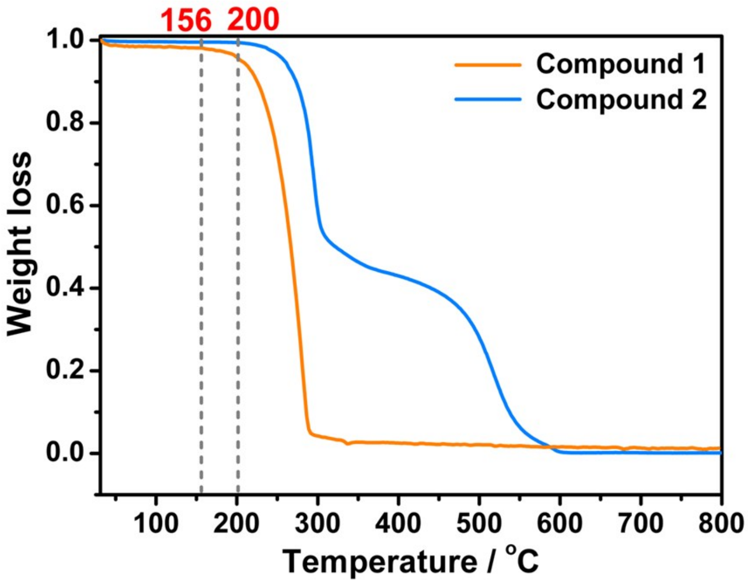

Fig. S2 TG curves of **1** and **2** under N_2 atmosphere.

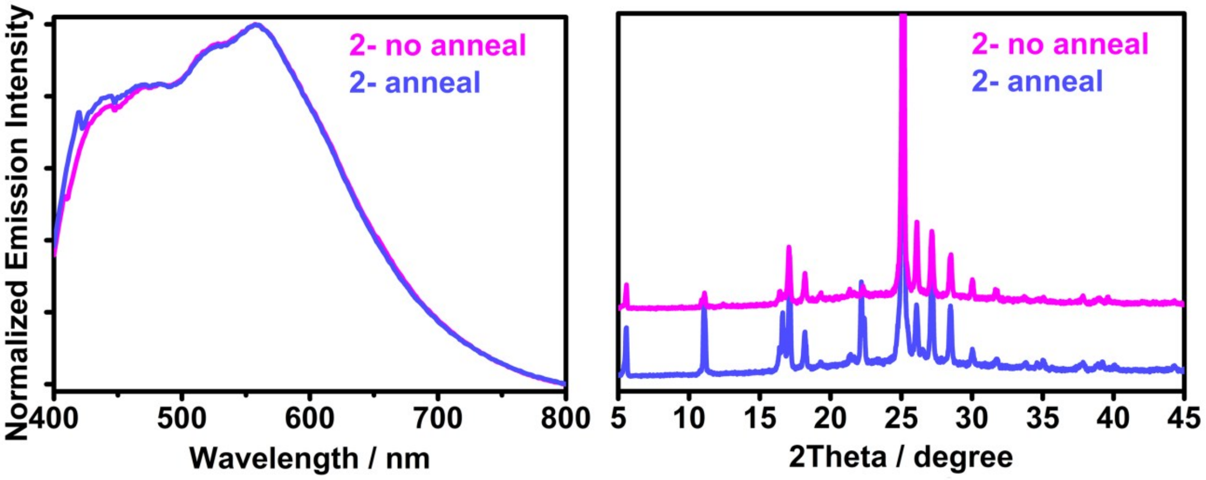

Fig. S3 Photoluminescence spectra (left; λ_{ex} = 370 nm) and PXRD patterns (right) for one crystalline sample of **2** before and after annealing at 150 °C for 1 d.

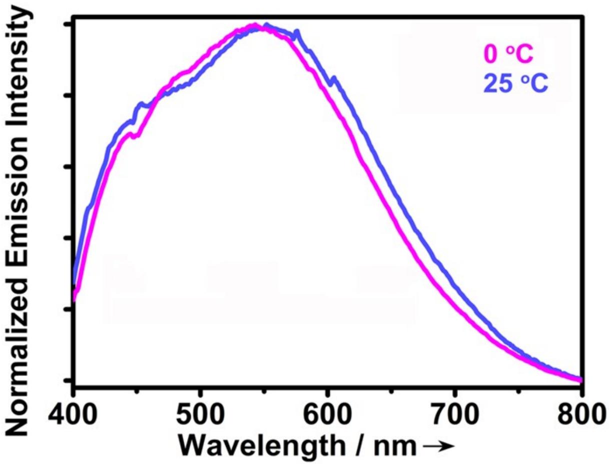

Fig. S4 Photoluminescence spectra (λ_{ex} = 370 nm) of the crystals of **2** obtained by recrystallization in ethanol at different temperatures. Inset: photographs of the crystals.

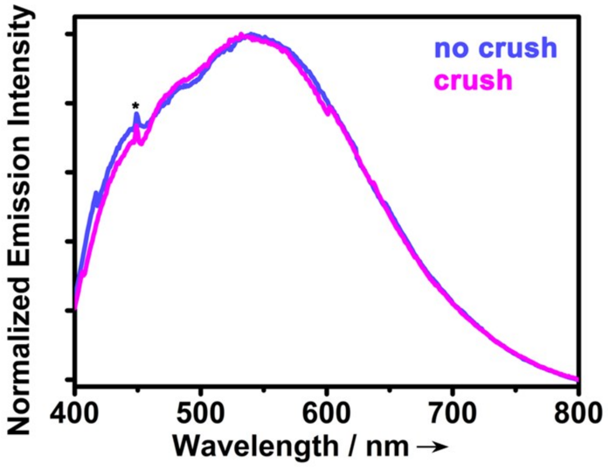

Fig. S5 Photoluminescence spectra (λ_{ex} = 370 nm) of the crystals of **2** before and after crushing. Note: The instrument noise is labelled as the * symbol.

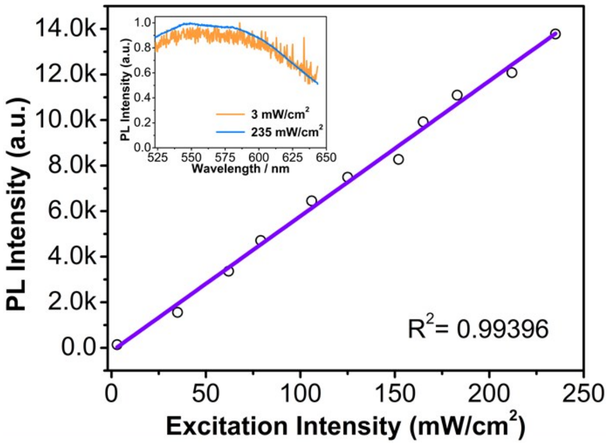

Fig. S6 Dependence of emission intensity at 560 nm of **2** on excitation intensity (3−235 mW/cm^2; black circle) at 293 K and a linear fit (purple line; λ_{ex} = 420 nm). Inset: emission profiles at excitation intensities of 3 and 235 mW/cm^2.

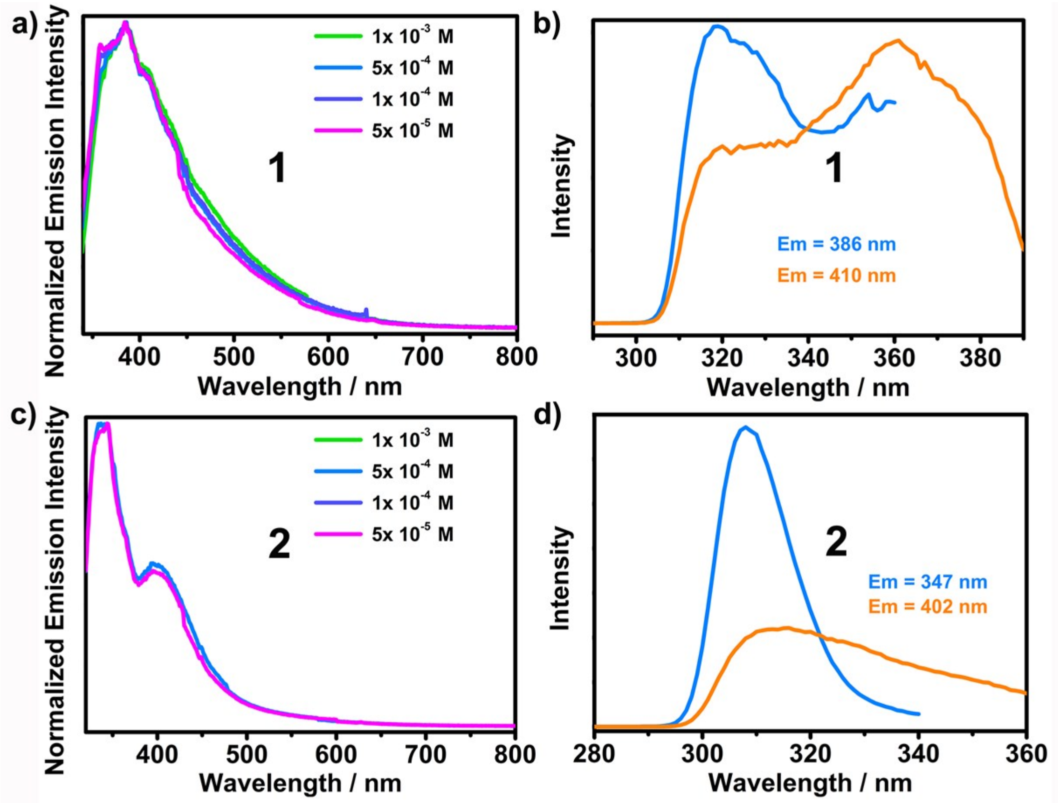

Fig. S7 (a) Emission spectra of **1** in DMF at different concentration under excitation at 315 nm; (b) excitation spectrum of **1** in DMF for emission at 386 and 410 nm; (c) emission spectra of **2** in DMF at different concentration under excitation at 320 nm; (d) excitation spectrum of **2** in DMF for emission at 347 and 402 nm. Upon increase in concentration from 5 × 10^{-5} to 1 × 10^{-3} M, no new emission peaks emerged, implying that excimer emission for **1** and **2** in the crystalline state can be excluded.

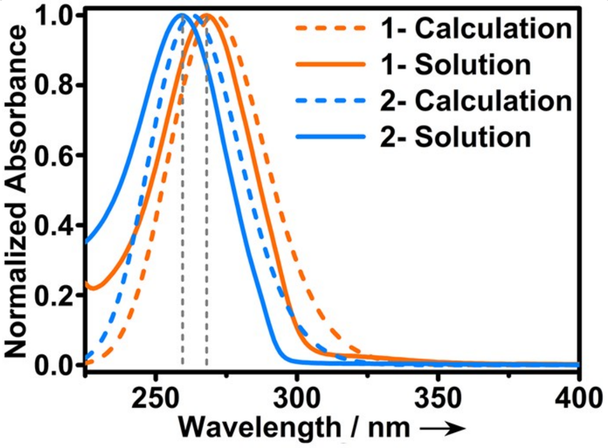

Fig. S8 Experimental (5×10^{-5} M DMF solution; solid lines) and calculated (TD-DFT, B3LYP/6-31G(d,p), monomer; dash lines) UV–Vis absorption spectra of **1** and **2**.

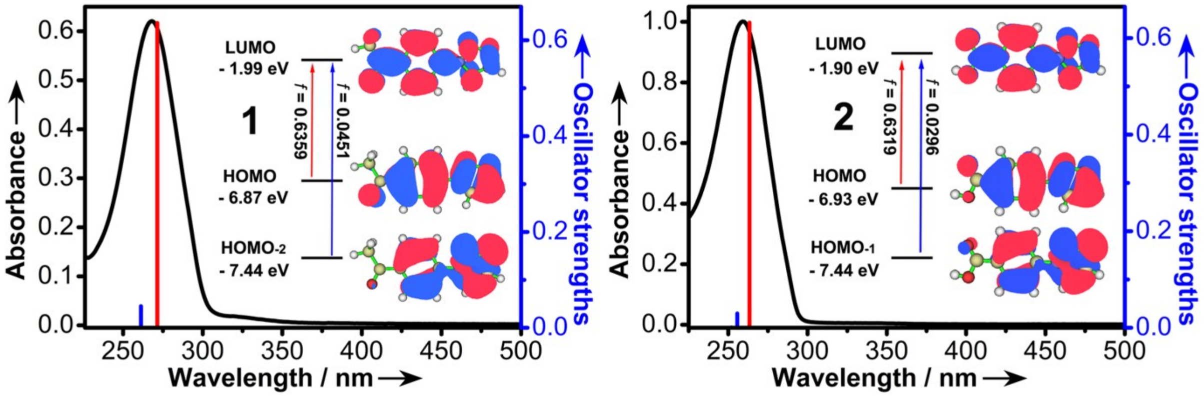

Fig. S9 Normalized experimental UV–Vis absorption spectra of **1** (a) and **2** (b) in 5×10^{-5} M DMF (black curves, left axis), oscillator strengths (*f*; vertical lines, right axis) obtained by the TD–DFT calculation at the B3LYP/6-31G(d,p) level and the corresponding frontier molecular orbitals (inset). The detailed calculation results are listed in Table S2. As can been seen, the absorption originates mainly from the HOMO → LUMO transition.

Table S2. TD-DFT calculations at the B3LYP/6-31G(d,p) level for the monomers of **1** and **2** using optimized geometries.

Electronic transitions $S_0 \rightarrow S_1$	λ^{abs}_{max} (nm)	Oscillator strength, *f*	Excitation energies (eV)	Main configurations
1	271.33	0.6359	4.5695	HOMO → LUMO
	261.01	0.0451	4.7503	$HOMO_{-2} \rightarrow LUMO$
2	263.22	0.6319	4.7103	HOMO → LUMO
	255.52	0.0296	4.8521	$HOMO_{-1} \rightarrow LUMO$

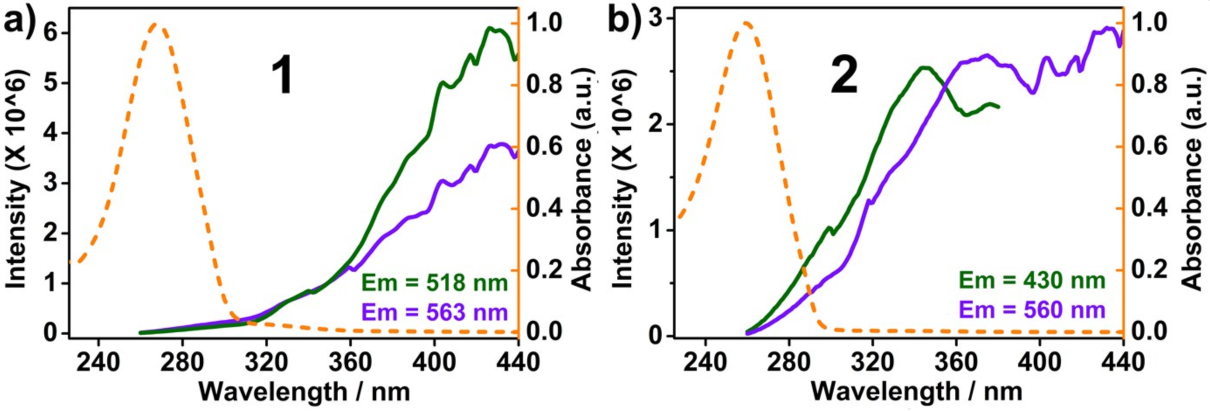

Fig. S10 Excitation spectra of **1** (a) and **2** (b) in the solid state. The absorption profiles (orange dash lines) in diluted DMF solution are also shown for comparison.

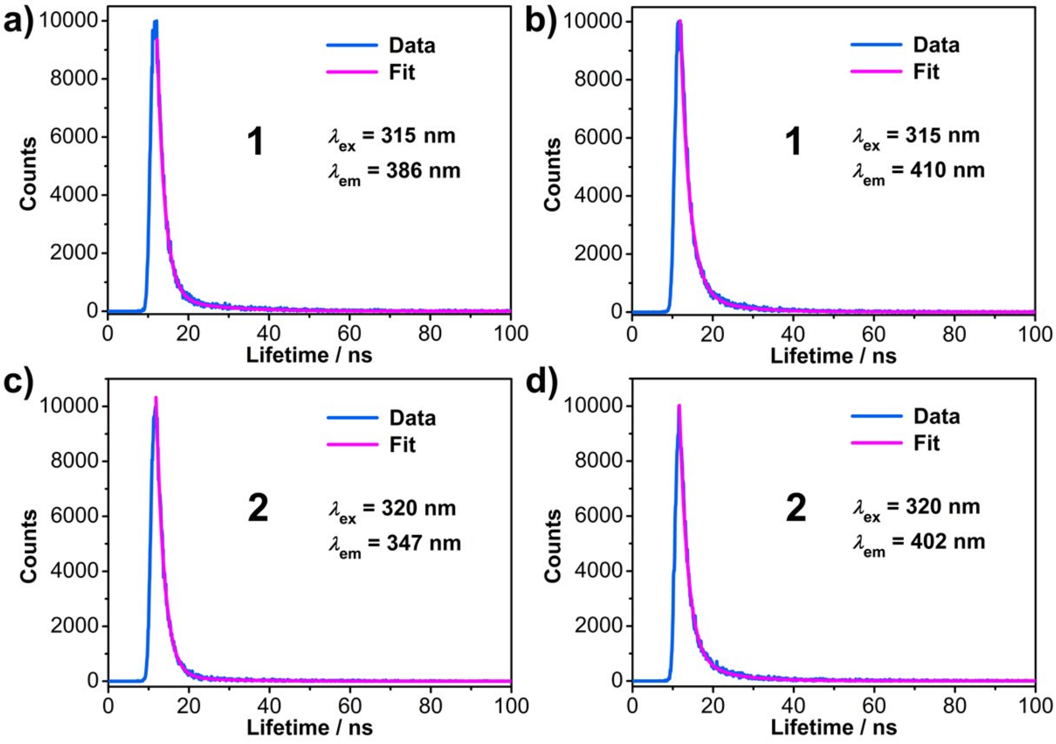

Fig. S11 (a-b) Photoluminescence lifetime profiles of **1** measured in the DMF solution (1×10^{-3} M) at 298 K ($\tau_{386\ nm}$ = 1.97 × 74.04% + 12.23 × 25.96%= 4.63 ns; $\tau_{410\ nm}$ = 2.33 × 76.82% + 9.91 × 23.18% = 4.08 ns). (c-d) Photoluminescence lifetime profiles of **2** measured in the DMF solution (1×10^{-3} M) at 298 K ($\tau_{347\ nm}$ = 2.04 × 89.83% + 12.87 × 10.17% = 3.14 ns; τ_{402nm} = 2.10 × 68.48% + 8.41 × 31.52% = 4.09 ns).

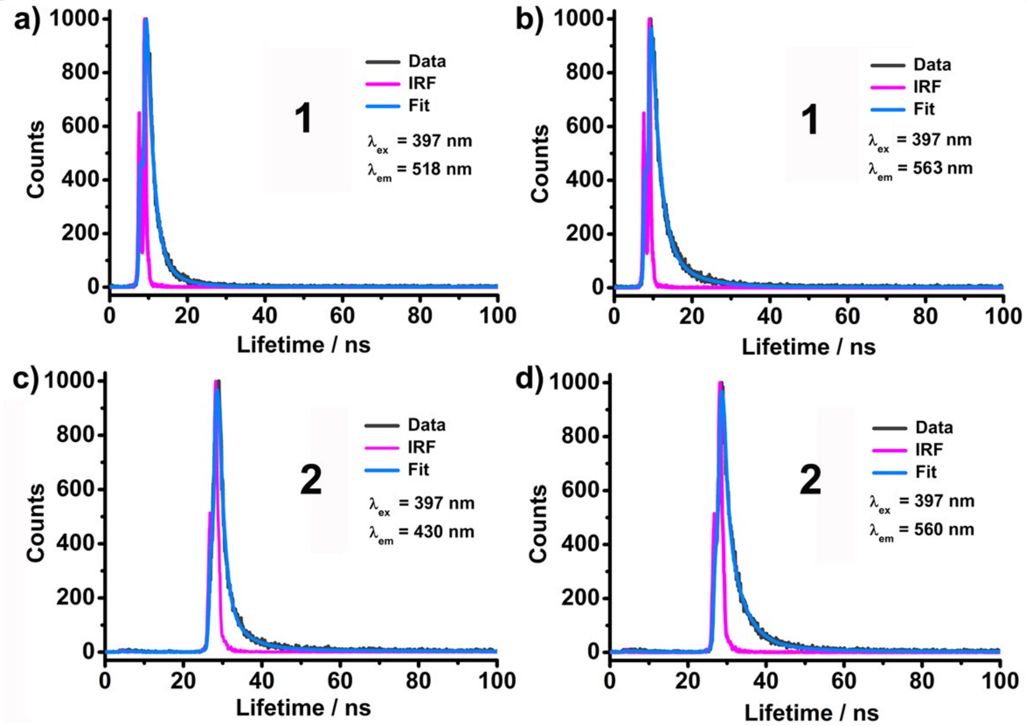

Fig. S12 (a-b) Photoluminescence lifetime profiles of **1** measured in the solid state at 298 K ($\tau_{518\ \mathrm{nm}}$ = 1.663 × 75.61% + 5.595 × 24.39%= 3.34 ns; $\tau_{563\ \mathrm{nm}}$ = 2.076 × 65.64% + 7.68*34.36% = 3.10 ns). (c-d) Photoluminescence lifetime profiles of **2** measured in the solid state at 298 K ($\tau_{430\ \mathrm{nm}}$ = 1.131 × 57.18% + 4.909 × 31.36% + 41.69 × 11.45%= 4.97 ns; $\tau_{560\mathrm{nm}}$ = 0.7901 × 28.99% + 4.194 × 59.69% + 18.61 × 11.32% = 2.40 ns).

Table S3. Crystal data and structural refinements for **1** and **2**.

	1	**2**
Formula	$C_{10}H_9N_3O$	$C_9H_7N_3O_2$
Mr	187.20	189.18
Crystal size (mm^3)	0.33 × 0.21 × 0.08	0.35 × 0.25 × 0.08
Crystal system	Monoclinic	Monoclinic
Space group	$P2_1/c$	$P2_1/c$
a **(Å)**	4.0292(4)	4.8058(2)
b **(Å)**	20.910(2)	5.4704(3)
c **(Å)**	10.8794(12)	31.7944(16)
α **(deg)**	90	90
β **(deg)**	96.641(17)	90.687(4)
γ **(deg)**	90	90
V **(Å^3)**	910.6(2)	835.80(7)
D_{calcd} **(g/cm^3)**	1.366	1.503
Z	4	4
F(000)	392	392
Abs coeff (mm^{-1})	0.759	0.929
R_1[a]	0.1565[c]	0.0420
ωR_2[b]	0.4744	0.1354
GOF on F^2	1.221	1.038

---

[a] $R_1 = \Sigma||F_o|–|F_c||/\Sigma|F_o|$; [b] $\omega R_2 = \{\Sigma\omega[(F_o)^2–(F_c)^2]^2/\Sigma\omega[(F_{o})_2]^2\}^{1/2}$.

[c] The crystal of **1** with satisfied quality was difficultly obtained, although various methods, such as recrystallization and volatilization, have been tried. However, the structural model should be basically reasonable because of the accordance of experimental and simulated PXRD patterns (Fig. S24). The phase purity was also demonstrated by determination of NMR spectra (^{1}H: Fig. S20 and ^{13}C: Experimental Section shown above), mass spectra (MS; Fig. S22), thermogravimetric (TG) data (Fig. S2), X-ray powder diffraction (PXRD) data (Fig. S24), IR data (Experimental Section shown above), and elemental analysis data (Experimental Section shown above).

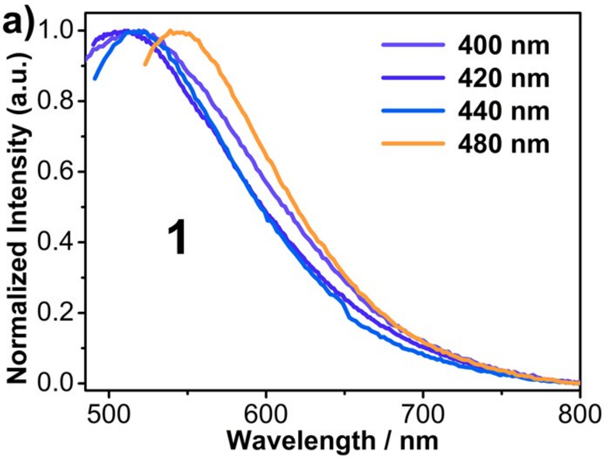

Fig. S13 Emission spectra of **1** and **2** under excitation at different wavelengths (400 → 480 nm) in the solid state. High pass filters used for measurement: 420 nm (385–485 nm) for λ_{ex} = 400 nm; 455 nm (438–490 nm) for λ_{ex} = 420 and 440 nm; 495nm (477–523 nm) for λ_{ex} = 480 nm.

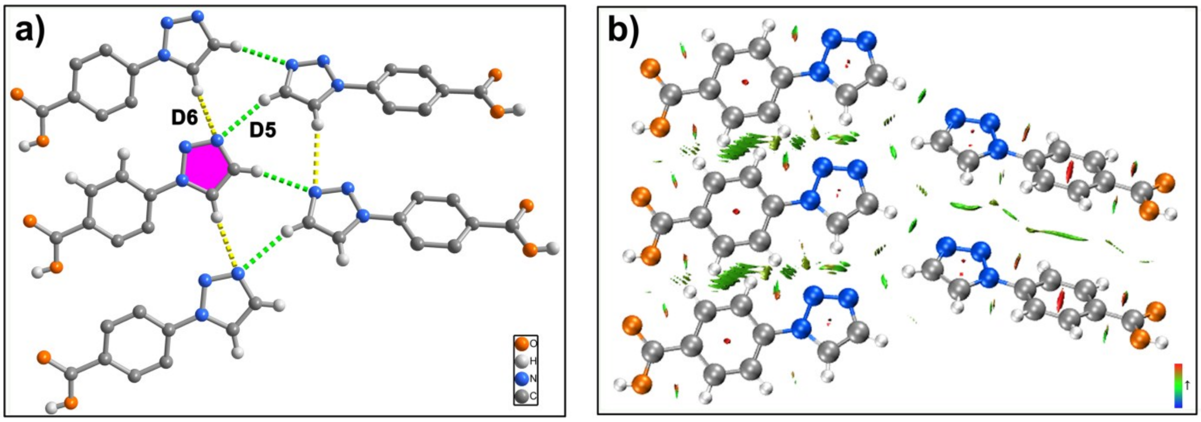

Fig. S14 a): C–H···N H-bonding interactions between one monomer and its neighbours for **2**. The H···N distances: D5 (green dash lines) = 2.54(2) Å; D6 (yellow dash lines) = 2.70(2) Å. This five H-bonded aggregate is the Gaussian calculation model of **2_H-pentamer** shown in Fig. S11. b): Gradient isosurfaces (s = 0.5 a.u.) for **2_H-pentamer**, The surfaces are colored on a blue-green-red (BGR) scale according to values of sign(λ_2)ρ, ranging from –0.04 to 0.02 a.u.. Blue indicates strong attractive interactions, and red indicates strong nonbonded overlap.

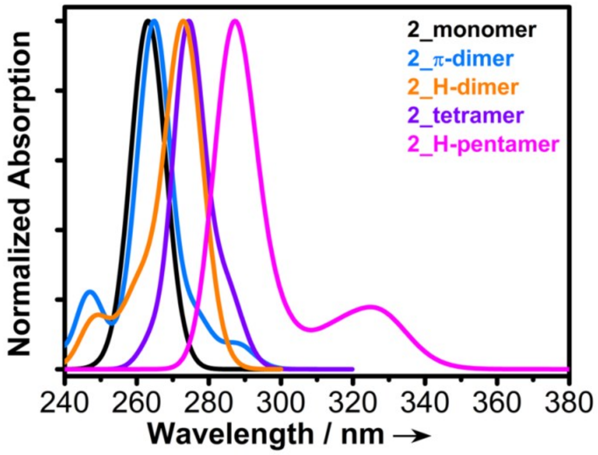

Fig. S15 UV–Vis absorption spectra of the monomer and different aggregates in the crystal of **2** obtained by TD-DFT calculations at the B3LYP/6-31+G(d,p) level.

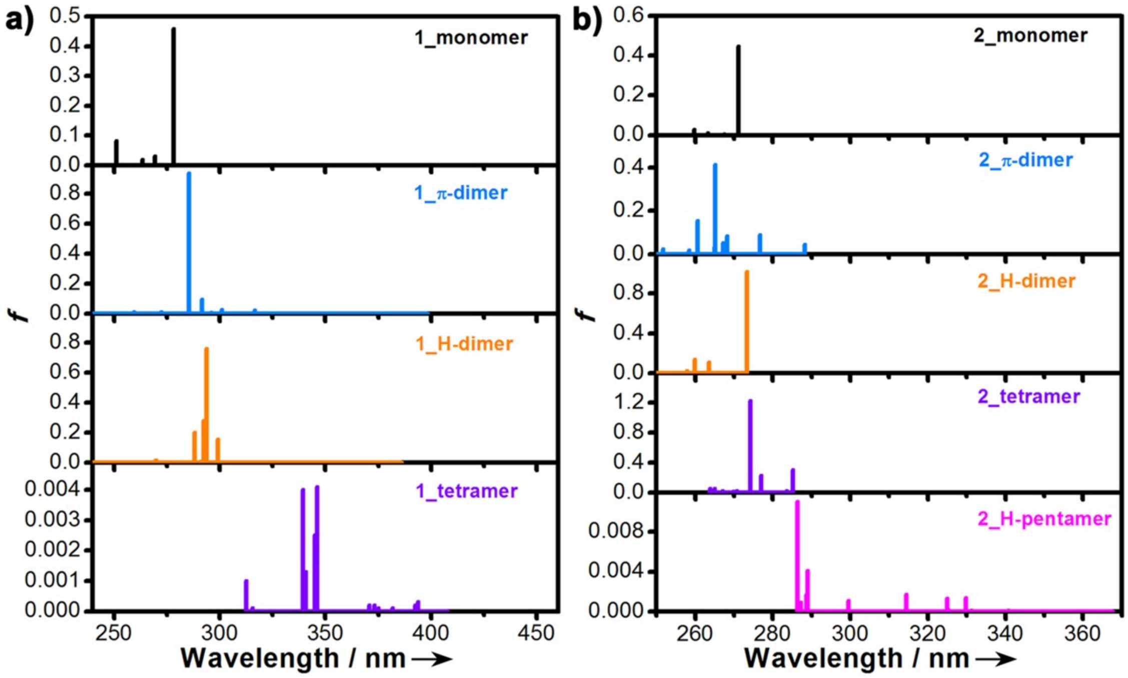

Fig. S16 Oscillator strengths (*f*) of the monomers and different aggregates in the crystals of **1** and **2** obtained by TD–DFT calculations at the B3LYP/6-31G(d,p) level.

Table S4. TD-DFT computations at the B3LYP/6-31+G(d,p) level for the selected structural fragments of **1** and **2** shown in **Fig. 5** in the manuscript and **Fig. S11**.

Electronic transitions $S_0 \rightarrow S_1$	**λ^{abs}_{max} (nm)**	**Oscillator strength, *f***	**Excitation energies (eV)**	**Main configurations**
1_monomer	278.23	0.4575	4.4562	HOMO → LUMO
	251.04	0.0812	4.9387	HOMO$_{-3}$ → LUMO
1_π-dimer	316.45	0.0254	3.9180	HOMO$_{-1}$ → LUMO$_{+1}$
	291.60	0.0965	4.2519	HOMO$_{-4}$ → LUMO$_{+1}$
	285.26	0.9343	4.3463	HOMO$_{-3}$ → LUMO

1_H-dimer	293.67	0.7563	4.2220	HOMO$_{-1}$ → LUMO$_{+1}$
	292.34	0.2804	4.2411	HOMO$_{-2}$ → LUMO
1_tetramer	345.98	0.0041	3.5836	HOMO$_{-4}$ → LUMO
	344.80	0.0025	3.5959	HOMO → LUMO$_{+2}$
	340.53	0.0013	3.6409	HOMO$_{-3}$ → LUMO
2_monomer	270.93	0.4466	4.5762	HOMO → LUMO
	259.61	0.0268	4.7758	HOMO$_{-3}$ → LUMO
2_π-dimer	276.54	0.0890	4.4834	HOMO$_{-1}$ → LUMO$_{+1}$
	268.13	0.0823	4.6241	HOMO$_{-2}$ → LUMO$_{+1}$
	265.01	0.4124	4.6785	HOMO$_{-1}$ → LUMO$_{+1}$
2_H-dimer	273.15	1.0143	4.5391	HOMO → LUMO
	263.34	0.1118	4.7082	HOMO$_{-1}$ → LUMO$_{+1}$
2_tetramer	285.05	0.3010	4.3495	HOMO$_{-1}$ → LUMO
	276.79	0.2252	4.4793	HOMO$_{-2}$ → LUMO
	274.08	1.2249	4.5236	HOMO$_{-2}$ → LUMO
2_H-pentamer	340.56	0.0001	3.6406	HOMO → LUMO$_{+1}$
	329.64	0.0014	3.7612	HOMO$_{-1}$ → LUMO$_{+1}$
	324.79	0.0013	3.8173	HOMO → LUMO$_{+2}$

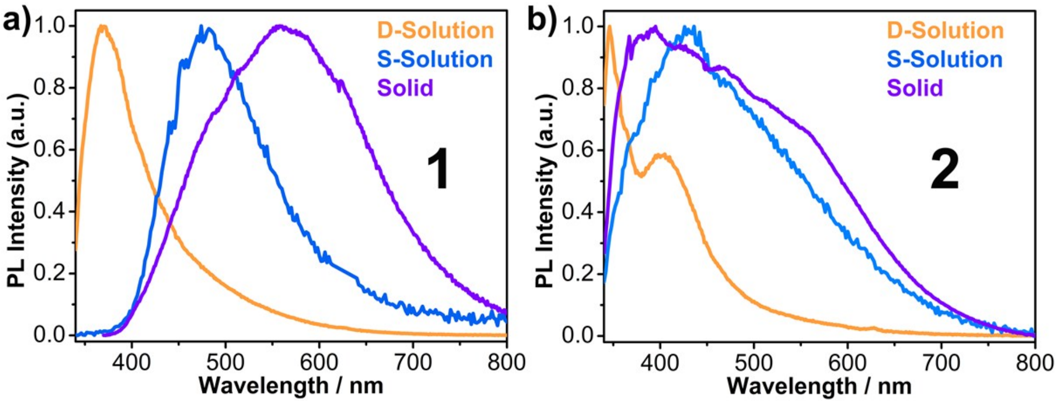

Fig. S17 The emission profiles of diluted DMF solution (D-Solution) (5×10^{-5} M), saturated DMF solution (S-Solution) and solid state of **1** (a) and **2** (b) at λ_{ex} = 320 nm. Saturated DMF solution was obtained by dissolving excess sample to 2 ml DMF and then filtrating at room temperature.

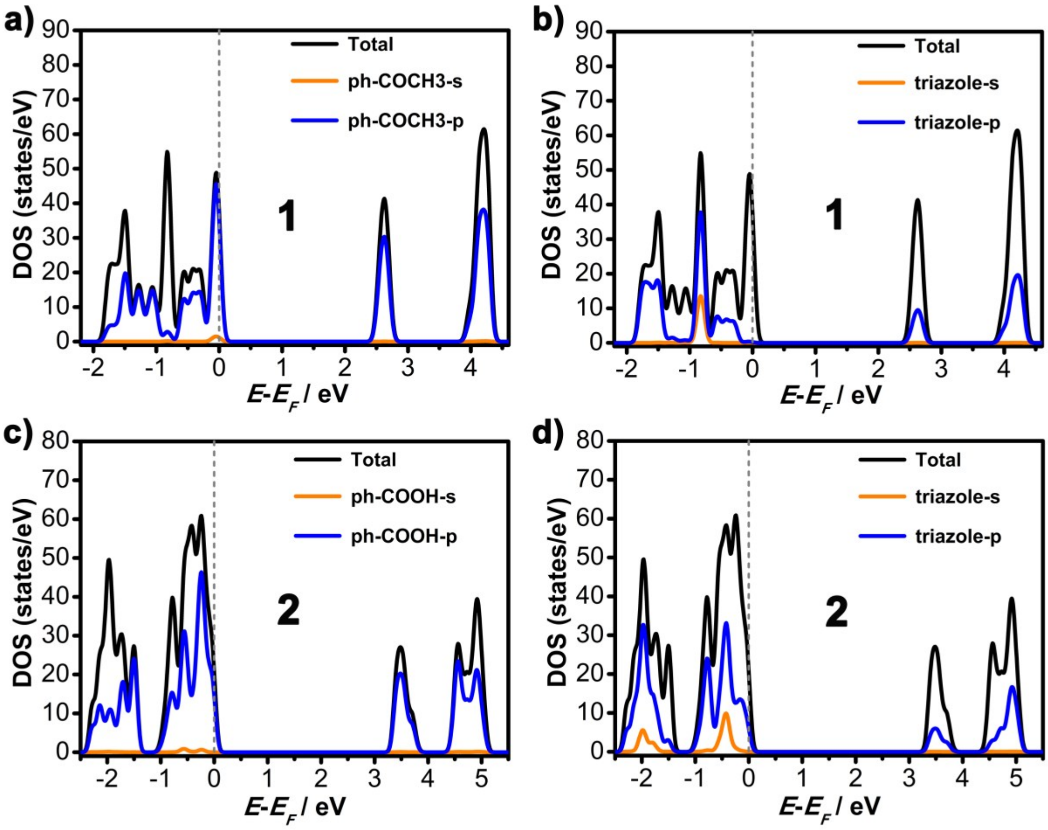

Fig. S18 Total and partial density of state (DOS) of **1** and **2**. The Fermi level (E_F) is set to zero by default (grey dashes). ph = phenyl.

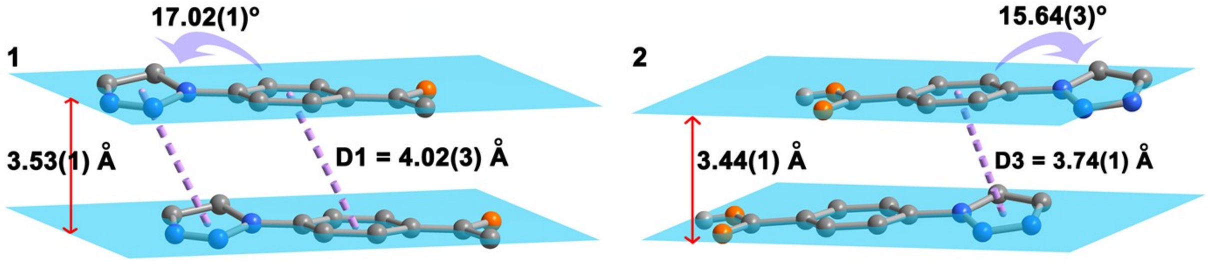

Fig. S19 Structures of two π-staked monomers for **1** and **2**. Interplanar distances of two monomers, centroid-to-centroid separations between two π-staked rings, and torsion angles between benzene and triazole in one monomer are labeled.

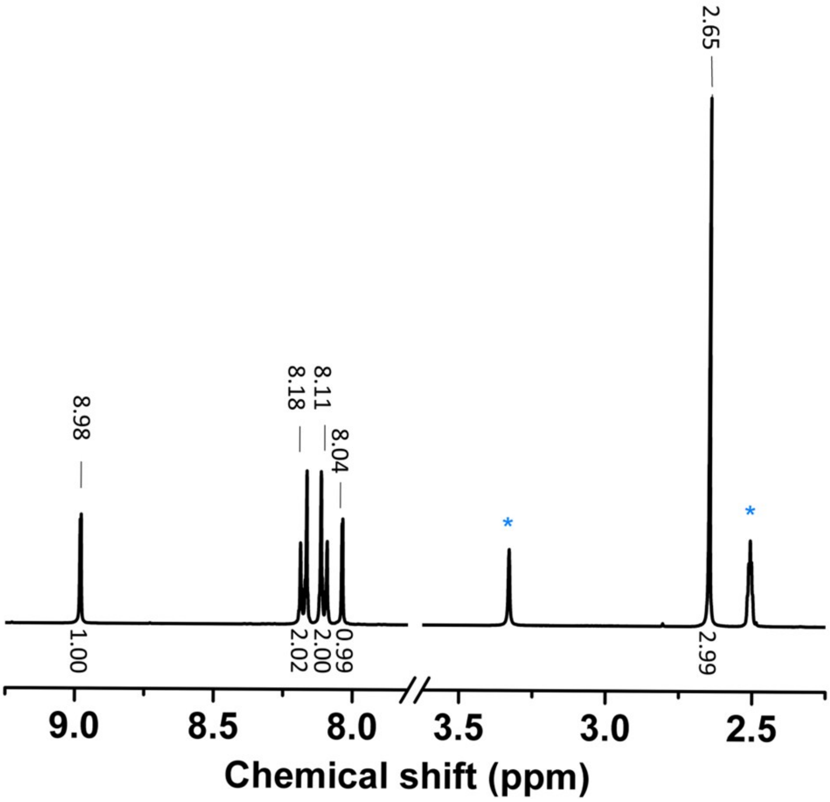

Fig. S20. ^{1}H-NMR spectrum of **1** in d_6-DMSO. The solvent and water peaks are marked with asterisks.

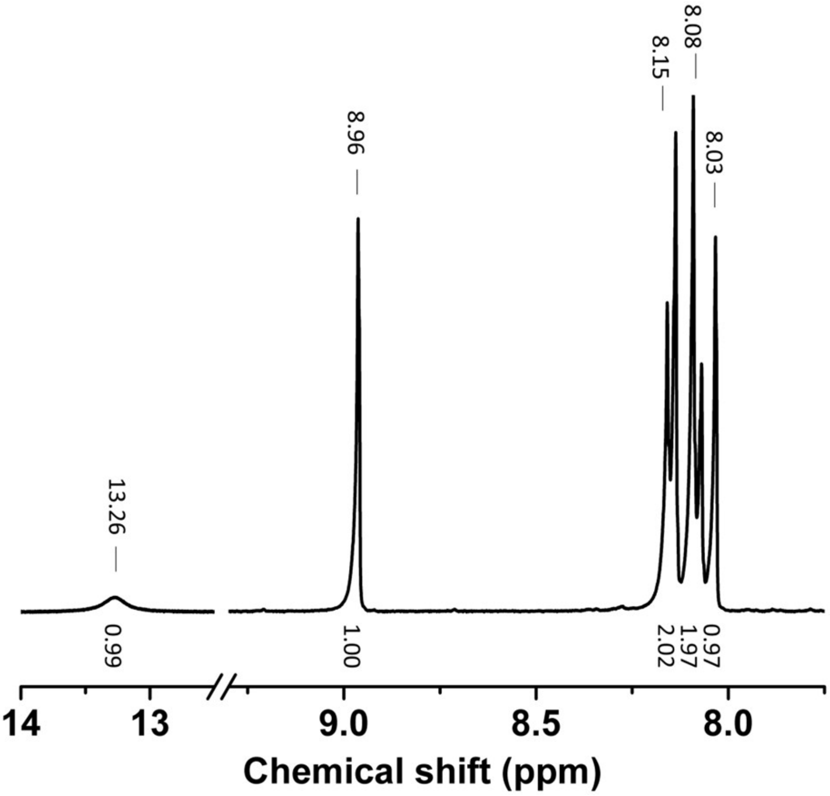

Fig. S21 ^{1}H-NMR spectrum of **2** in d_6-DMSO.

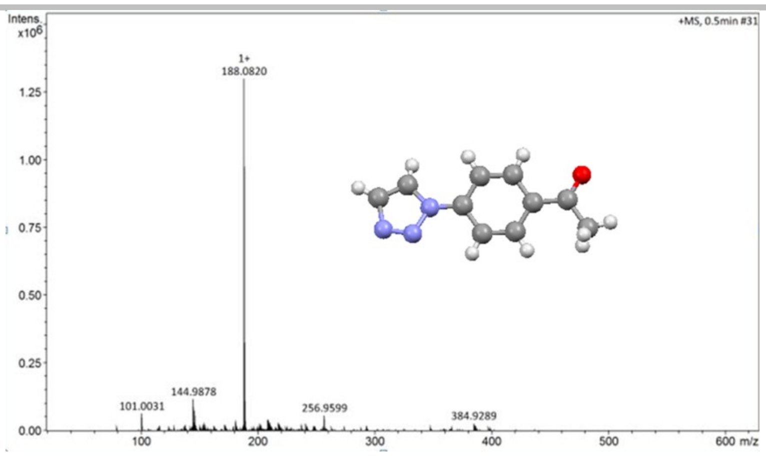

Fig. S22. Mass spectra of **1**.

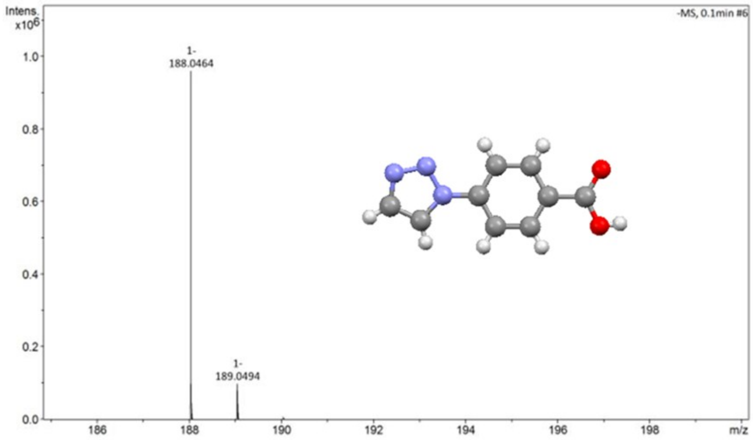

Fig. S23 Mass spectra of **2**.

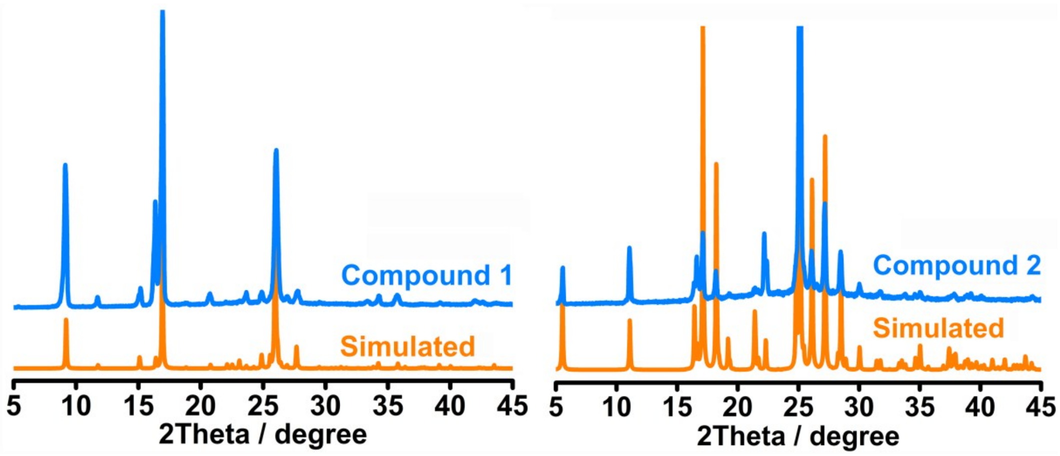

Fig. S24 Experimental and simulated PXRD patterns of **1** and **2**.

References

1 J. T. B. Kueh, K. W. Choi and M. A. Brimble, *Org. Biomol. Chem.*, 2012, **10**, 5993–6002.

2 E. R. Dohner, A. Jaffe, L. R. Bradshaw and H. I. Karunadasa, *J. Am. Chem. Soc.*, 2014, **136**, 13154-13157.

3 CrysAlisPro, *Agilent Technologies*, Version 1. 171. 37. 33, 2014..

4 Siemens. *SAINT and SHELXTL.*, Siemens Analytical X-ray Instruments Inc., Madison, Wisconsin, USA, 1994.

5 A. L. Spek, *PLATON.*, Utrecht University: Utrecht, The Netherlands, 2001.

6 Gaussian 09, Revision A.02, M. J. Frisch,; G. W. Trucks,; H. B. Schlegel, G. E. Scuseria, M. A. Robb, J. R. Cheeseman, G. Scalmani, V. Barone, B. Mennucci, G. A. Petersson, H. Nakatsuji, M. Caricato, X. Li, H. P. Hratchian, A. F. Izmaylov, J. Bloino, G. Zheng, J. L. Sonnenberg, M. Hada, M. Ehara, K. Toyota, R. Fukuda, J. Hasegawa, M. Ishida, T. Nakajima, Y. Honda, O. Kitao, H. VrevenT. Nakai, J. A., Jr. Montgomery, J. E. Peralta, F. Ogliaro, M. Bearpark, J. J. Heyd, E. Brothers, K. N. Kudin, V. N. Staroverov, R. Kobayashi, J. Normand, K. Raghavachari, A. Rendell, J. C. Burant, S. S. Iyengar, J. Tomasi, M. Cossi, N. Rega, J. M. Millam, M. Klene, J. E. Knox, J. B. Cross, V. Bakken, C. Adamo, J. Jaramillo, R. Gomperts, R. E. Stratmann, O. Yazyev, A. J. Austin, R. Cammi, C. Pomelli, J. W. Ochterski, R. L. Martin, K. Morokuma, V. G. Zakrzewski, G. A. Voth, P. Salvador, J. J. Dannenberg, S. Dapprich, A. D. Daniels, O. Farkas, J. B. Foresman, J. V. Ortiz, J. Cioslowski and D. J. Fox, *Gaussian, Inc.*, Wallingford CT, 2009.

7 C. T. Lee, W. T. Yang and R. G. Parr, *Phys. Rev. B.*, 1988, **37**, 785-789.

8 L. A. Curtiss, P. C. Redfern, K. Raghavachari and J. A. Pople, *J. Chem. Phys.*, 2001, **114**, 108-117.

9 E. R. Johnson, S. Keinan, P. Mori-Sánchez, J. Contreras-García, A. J. Cohen, and W. T. Yang, *J. Am. Chem. Soc.*, 2010, **132**, 6498-6506.

10 T. Lu and F. W. Chen, *J. Comput. Chem.*, 2012, **33**, 580-592.

11 S. J. Clark, M. D. Segall, C. J. Pickard, P. J. Hasnip, M. I. J. Probert, K. Refson and M. C. Payne, *Z. Kristallogr. - Cryst. Mater.,* 2005, **220**, 567-570.

12 a) B. Hammer, L. B. Hansen and J. K. Norskov, *Phys. Rev. B: Condens. Matter Mater. Phys.*, 1999, **59**, 7413-7421; b) J. P. Perdew and Y. Wang, *Rev. B: Condens. Matter Mater. Phys.*, 1992, **45**, 13244-13249.

13 a) D. R. Hamann, M. Schlüter and C. Chiang, *Phys. Rev. Lett.*, 1979, **43**, 1494-1497; b) J. S. Lin, A. Qteish, M. C. Payne and V. Heine, *Phys. Rev. B: Condens. Matter Mater. Phys.*, 1993, **47**, 4174-4180.

14 F. Bassani and G. P. Parravicini, *Electronic States and Optical Transitions in Solids*; Pergamon Press Ltd.: Oxford, U.K., 1975.

15 Y. Li, W. Q. Zou, M. F. Wu, J. D. Lin, F. K. Zheng, Z. F. Liu, S. H. Wang, G. C. Guo and J. S. Huang, *CrystEngComm*, 2011, **13**, 3868-3877.

16 H. Y. Rienhoff, J. M. McCall, M. Clare, C. Celatka and A. E. Tapper, U.S. Patent Application 15/043,121, 2016, 2-12.